Nuclear Engineering Education Research (NEER) Program

Final Report

Project Title: Hierarchical Adaptive Solution of Radiation Transport Problems on Unstructured Grids

Covering Period: August 8, 2004 through August 8, 2007

Recipient: Georgia Tech Research Corporation
Office of Sponsored Programs
Georgia Institute of Technology
505 Tenth Street, N.W.
Atlanta, GA – 30332-0420

Award Number: DE-FG07-04ID14604

Contact: Dr Cassiano R E de Oliveira
Nuclear and Radiological Engineering Program
George W. Woodruff School of Mechanical Engineering
Atlanta, GA – 30332-0405
1-404-385-4928 Voice
1-404-894-3733 Fax
c.oliveira@gatech.edu

Project team: Seb Klein
Department of Energy
Idaho Operations Office
1955 Fremont Avenue
Idaho Falls, Idaho 83401-1221

Hierarchical Adaptive Solution of Radiation Transport Problems on Unstructured Grids

DOE NEER Award DE-FG07-04ID14604

Principal Investigator:
Dr Cassiano R. E. de Oliveira,
Nuclear Engineering and Radiological & Medical Physics Program,
GWW School of Mechanical Engineering,
Georgia Institute of Technology, Atlanta, GA 30332-0405

1. Motivation and Project Objectives

Computational radiation transport has steadily gained acceptance in the last decade as a viable modeling tool due to the rapid advancements in computer software and hardware technologies. It can be applied for the analysis of a wide range of problems which arise in nuclear reactor physics, medical physics, atmospheric physics, astrophysics and other areas of engineering physics. However, radiation transport is an extremely challenging computational problem since the governing equation is seven-dimensional (3 in space, 2 in direction, 1 in energy, and 1 in time) with a high degree of coupling between these variables. If not careful, this relatively large number of independent variables when discretized can potentially lead to sets of linear equations of intractable size. Though parallel computing has allowed the solution of very large problems, available computational resources will always be finite due to the fact that ever more sophisticated multiphysics models are being demanded by industry. There is thus the pressing requirement to optimize the discretizations so as to minimize the effort and maximize the accuracy.

One way to achieve this goal is through adaptive phase-space refinement. Unfortunately, the quality of discretization (and its solution) is, in general, not known *a priori*; accurate error estimates can only be attained via the *a posteriori* error analysis. In particular, in the context of the finite element method, the *a posteriori* error analysis provides a rigorous error bound. The main difficulty in applying a well-established *a posteriori* error analysis and subsequent adaptive refinement in the context of radiation transport is the strong coupling between spatial and angular variables.

This project was concerned with the adaptive solution of the radiation transport equation on unstructured grids. The specific aims, as outlined in the research proposal, were: to exploit multiresolution in space and on the sphere, to develop an adaptive hierarchical space/angle algebraic preconditioner for the solution for the adapted space-angle equations, and to investigate suitable error measures for radiation flux to be used by the adaptivity algorithms.

2. Summary of Yearly Research Progress

In the first year of the project work concentrated on (a) the development of the algebraic multigrid method using the existing finite element-spherical harmonics framework; and (b) adaptive space and angle refinement methods. It was decided to place emphasis on the algebraic

multigrid method instead of spherical wavelets for the angular resolution since the development of the robust solution algorithm was more crucial to solve practical problems. Work on multiresolution on the sphere using spherical wavelets was postponed to years 2 and 3.

In the first year of the project work concentrated on: (a) the development of an algebraic multigrid method using the existing finite element-spherical harmonics framework; and (b) adaptive angular resolution methods. As a result of the first year work, an algebraic multigrid preconditioner was developed which takes into account a special structure of finite element-spherical harmonics matrices. The method reduces its storage requirements by taking into account tensorial nature of the matrix, and numerical results showed a scalable computation time. Two conference papers were published in the ANS Transactions [**1,2**] and in the Proceedings the 2005 ANS Topical Meeting of Mathematics and Computation Division [**3**].

For the adaptive space and angular refinement strategy, the spatial anisotropic refinement module was implemented in the code EVENT. An adaptive nodal-wise angular refinement algorithm was developed using the hierarchical nature of spherical harmonics expansions. The method successfully refines the angular expansion, and the same accuracy for a quantity of interest (i.e. multiplication factor k-effective) was obtained with much smaller number of degrees of freedom. In this regard, we have published the summary paper in the Transactions of the ANS [**4**], and the general adaptive strategy was presented in the 19th International Transport Theory Conference [**5**].

In the second and third year, work focused on the development of a rigorous space-angle coupled adaptive framework. The adaptive framework utilizes the residual-based *a posteriori* error analysis. As a result, *a posteriori* error estimators were developed for both spatial and angular discretization error based on the unified framework. The error indicators were developed to identify the global L_2 and energy norms, which are computed by the simple local finite element solutions. The space-angle coupled adaptive refinement procedure is done with an aid of *a posteriori* error estimators.

As the next step, an alternative approach was sought for the adaptive framework, which considers the minimization of error in the engineering output rather than the global norm. This approach, also known as "goal-oriented adaptivity", utilizes the dual argument of the problem to characterize the error in the desired engineering output. The product of forward and adjoint error provides the error bounds for the arbitrary functional output. Our approach to the goal-oriented adaptivity closely follows the methodology developed by others, however, we obtained different error bounds by integrating *a posteriori* error analysis and the well-known extremum variational principles. Conference papers were published in the ANS Transactions [**6,7**], in the Proceedings of the 2007 ANS topical meeting of the Mathematics and Computation Division [**8**], and two journal papers were produced [**9,10**]

3. The Algebraic Multigrid Method

3.1 Introduction

The accurate solution for practical 3D problems requires the large number of space-angle degrees of freedom, whose solution algorithm is perforce iterative. A robust solution scheme is, therefore, a vital tool for successfully solving such large complex problems. Krylov subspace methods such as the preconditioned conjugate gradient (PCG) are commonly used in the iterative solution but their performance is highly dependent on the preconditioning strategy. The choice of the preconditioner is thus the most important aspect for the practical implementation of Krylov methods.

An alternative to the PCG is the multigrid (MG) method [**11**], which has been shown to be a very efficient elliptic partial differential equation (PDE) solver. The MG uses the fact that the simple relaxation works well for the high-frequency errors. Therefore, the MG method creates the different (hierarchical) levels of discretized systems, and tries to capture all levels of frequencies by a few simple relaxations. We have applied the algebraic multigrid (AMG) method to the solution of the even-parity finite element-spherical harmonics (FE-P_N) method which has been implemented in the EVENT code [**12**]. The objective of the task is to develop a hierarchical multilevel preconditioning technique to efficiently solve the space-angle coupled system of equations

In order to apply the MG concept to the space-angle finite element matrices, work was separated into two steps. In the first step, the AMG preconditioner was applied to solve each of the diagonal FE-P_N matrices in the symmetric block Gauss-Seidel (SSOR(1)) preconditioning stage of the Moment-by-Moment (MBM) PCG procedure [**1**]. In the second step, we have extended the concept of the AMG to solve the whole FE-P_N matrix using a point-based approach as the alternative of the MBM preconditioner [**2**].

3.2 Numerical Methodology and Results

The deterministic radiation transport code EVENT is based on the second-order, even-parity form of the transport equation. The Ritz-Galerkin procedure applied to the even-parity form of the transport equation using finite elements in space and spherical harmonics in angle yields for each energy group a coupled system of equations of the form [**13**]:

$$\boldsymbol{A}\boldsymbol{\Psi}=\mathbf{b} \tag{1}$$

where $\boldsymbol{A}$ is a $NM \times NM$ matrix, $\boldsymbol{\Psi}$ the $NM \times 1$ vector of space-moment unknowns, with N the number of nodes in the finite element mesh, and M the number of spherical harmonics moments in the expansion of the angular flux. The matrix $\boldsymbol{A}$ is symmetric, positive-definite and, due to the compact support of the finite element basis, sparse and often banded.

Although the matrix $\boldsymbol{A}$ is sparse due to the finite element discretization, for large problems its explicit assembly nevertheless becomes prohibitive. To overcome this, the strategy employed in EVENT is to partition the matrix $\boldsymbol{A}$ into $M \times M$ sub-matrices of dimension $N \times N$:

$$\boldsymbol{A} = \begin{pmatrix} \boldsymbol{A}_{11} & \boldsymbol{A}_{12} & .. & \boldsymbol{A}_{1M} \\ \boldsymbol{A}_{12}^{T} & \boldsymbol{A}_{22} & .. & .. \\ .. & .. & .. & \boldsymbol{A}_{M-1M} \\ \boldsymbol{A}_{1M}^{T} & .. & \boldsymbol{A}_{M-1M}^{T} & \boldsymbol{A}_{MM} \end{pmatrix} \tag{2}$$

where each block matrix $\boldsymbol{A_{ij}}$ contains the spatial finite elements connections. In this fashion, the preconditioned conjugate gradient (PCG) method can be naturally applied to solve this SPD system. A MBM-SSOR preconditioner is chosen of the form:

$$\boldsymbol{M} = (\boldsymbol{D} + \boldsymbol{L})\boldsymbol{D}^{-1}(\boldsymbol{D} + \boldsymbol{L}^{T}) \tag{3}$$

with

$$\boldsymbol{L}_{ij} = \begin{cases} \boldsymbol{A}_{ij} & if \;\; moment\; i > j \\ 0 & otherwise \end{cases} \qquad \boldsymbol{D}_{ij} = \begin{cases} \boldsymbol{A}_{ij} & if \;\; moment\; i= \\ 0 & otherwise \end{cases} \tag{4}$$

The MBM preconditioner requires only the diagonal angular sub-matrices being explicitly assembled. Operations involving the off-diagonal matrices are performed using the tensorial product nature of these matrices. The MBM-PCG solver has been implemented in EVENT which makes use of this partitioning [**14**].

The main drawback of the MBM preconditioner lies in the inversion of the block diagonal matrices. Each MBM preconditioning step requires the solution of 2*M*-1 matrix systems of order *N x N*. The computational cost of the MBM thus increases rapidly for the very large scale problems. In the light of this, a different preconditioning strategy, which posseses the scalability, needs to be considered.

It is well known that the MG preconditioner has very good performance for the elliptic problems. The basic concept of the MG is to reduce all the frequencies of errors simultaneously by using different mesh sizes. The high frequency errors, which correspond to the spatially localized errors, can be reduced effectively by a few classical iterations or relaxations on the fine grid. The low frequency errors, which have the long range, are eliminated by explicitly solving the coarse level matrix.

The AMG is suitable for unstructured mesh since the AMG uses only information of the matrix coefficients to generate the interpolation/restriction operators and the coarse level matrices. The classical AMG uses the concept of strong dependence to determine the directions in which low frequency errors propagate. The node *i* is said to be strongly depend on the node *j* if the following relationship holds:

$$-a_{ij} \geq \theta \max \left| a_{ik} \right| \tag{5}$$

The AMG uses the fact that low frequency errors vary slowly to the direction of strong dependence. The coarsening procedure is, therefore, performed in the direction of strong dependence. Eqn. (5) is used as a guidance to select the coarse nodal sets. The coarse level matrix is produced by the Galerkin condition:

$$A^{c} = P^{T} A P \tag{6}$$

where P is the prolongation operator and P^T is the restriction operator. It is possible to also use the AMG as a preconditioner of CG: one V-cycle sweep with a symmetric smoother (i.e. forward/backward GS, or Jacobi) can be used as a preconditioner. The algorithm for the MG V-cycle is shown in Figure 1.

(1)	Pre-smoothing:	$x'=RELAX(Ax=b)$
(2)	Calculate residual:	$r= b-Ax'$
(3)	Restrict residual:	$b^H= I^H_h r$
(4)	IF level = coarsest level: GO TO (5) ELSE GO TO (1)	$x^H=(A^H)^{-1}b^H$,
(5)	Prolongate solution:	$x^h= I^h_H x^H$
(6)	Post-smoothing:	$x^{h'} = RELAX(Ax=b)$
(7)	IF level = finest level GO TO (1), ELSE GO TO (5)	

Figure 1: MG V-cycle

The first step involved applying the AMG preconditioner to the spatial finite element matrix only (i.e. the AMG preconditioner was used to solve the diagonal block matrices for the MBM preconditioner.) [1]. The aim of this work is to improve the performance of the spatial preconditioning sweeps as preamble to the second step on a more general integrated hierarchical space-moment solution strategy. The numerical performance of the AMG preconditioner was compared with the commonly used preconditioners such as the SSOR(1) preconditioner and the incomplete Cholesky (ILU(0)) preconditioner.

In order to study the effectiveness of the AMG, two problems have been solved. The first problem considered consisted of a 2-dimensional, one-group, 5x5cm square region with Σ_t =1.0 cm^{-1}, and Σ_a=0.2 cm^{-1} and a uniformly distributed source. The second problem considered was the TN-12 Shipping Cask benchmark problem [**15**] (see Figure 2) which involved 22 groups and an outer iteration on the fission source. The number of the nodes in problem 1 and problem 2 are 160000 and 12250, respectively.

Figure 2. TN12 shipping cask geometry.

Table 1 shows the results of the test problems for the SSOR(1)/CG ILU(0)/CG, AMG/CG and a stand-alone AMG solver. Due to coding difficulties, it was not possible to produce results for Problem 2 using the stand-alone AMG solver. The first column shows the number of inner-most iterations, which correspond to the number of preconditioning stages in the PCG solution, or the number of V-cycles used in the stand-alone AMG. The third column shows the average number of inner iterations required per outer iteration (angular, group and fission source).

Table 1. Summary of Results for Test Problems

Ang. Expansion order	Method	# of inner iterations	# of outer iterations	inner/ outer	Sol. time (cpu secs)	AMG setup	Time per cycle
Problem #1 (# of nodes = 160000)							
P_1	SSOR(1)/CG	204	1	204	4.0		0.020
	ILU(0)/CG	154	1	154	3.8		0.024
	AMG/CG	9	1	9	0.7	6.25	0.078
	AMG stand-alone	14	1	14	0.9	6.7	0.064
P_3	SSOR(1)/CG	4602	64	72	118.4		0.025
	ILU(0)/CG	3351	64	52	86.9		0.026
	AMG/CG	282	64	4	24.9	26.2	0.088
	AMG stand-alone	225	64	4	18.5	26.1	0.082
P_5	SSOR(1)/CG	11567	154	75	348.8		0.030
	ILU(0)/CG	9198	154	60	224.3		0.024
	AMG/CG	758	154	5	92.9	60.37	0.123
	AMG stand-alone	537	154	3	64.1	60.71	0.119
Problem #2 (# of nodes = 12250)							
P_1	SSOR/CG	20841	132	158	182.5		0.009
	ILU(0)/CG	12524	132	95	110.6		0.009
	AMG/CG	1686	132	13	57.7	34.4	0.034
	AMG stand-alone	N/A	N/A	N/A	N/A	N/A	N/A

The results show the effectiveness of the AMG for reducing the number of inner iterations. Problem 1 required large number of inner iterations and the AMG/CG worked considerably

better than ILU(0)/CG both in terms of number of iterations and actual computational time. The stand-alone solver also worked very well for this problem. In Problem 2 the superiority of the AMG was not so clear because of two factors. Firstly the setup times for the hierarchical levels were significant due to the inefficient implementation of the coarse grid matrices generation scheme. This is currently being addressed and there is hope for considerable reduction of effort on this front. The second factor was that the required number of inner iterations steadily decreased as the outer angular and source iterations converged. The preconditioning stage of AMG is computationally 4~6 times more expensive compared to ILU(0). Thus the relative cost of AMG preconditioner became higher towards end of the computations.

The second step of this work is to develop a more general integrated hierarchical space-moment solution strategy [**2**]. The challenge is adapting the AMG concept into the system of PDEs. The approach taken here is so-called point-based AMG [**5**]. The point-based approach performs coarsening by using a representative matrix $\boldsymbol{B}$. The series of interpolation and restriction operators are generated by using the matrix $\boldsymbol{B}$. The coarse level matrix ($\boldsymbol{A}^C$) is then created by:

$$\begin{pmatrix} A_{11}^C & A_{12}^C & .. & A_{1M}^C \\ A_{21}^C & A_{22}^C & .. & .. \\ .. & .. & .. & .. \\ A_{M1}^C & .. & .. & A_{MM}^C \end{pmatrix} = \begin{pmatrix} P^T & 0 & .. & 0 \\ 0 & P^T & 0 & .. \\ .. & ... & ... & ... \\ 0 & .. & 0 & P^T \end{pmatrix} \begin{pmatrix} A_{11} & A_{12} & .. & A_{1M} \\ A_{21} & A_{22} & .. & .. \\ .. & .. & .. & .. \\ A_{M1} & .. & .. & A_{MM} \end{pmatrix} \begin{pmatrix} P & 0 & .. & 0 \\ 0 & P & 0 & .. \\ .. & ... & ... & ... \\ 0 & .. & 0 & P \end{pmatrix} \tag{7}$$

The diffusion matrix $\boldsymbol{A_{11}}$ is used as the representative matrix in the system. This choice was made because the slow convergence error comes from the diffusion matrix according to the Fourier analysis.

The tensorial nature of the FE-P_N matrices provides further simplification in the coarsening procedure. If coarse nodal points and the interpolation/restriction operators are fixed, the coarse level matrices for any moments can be generated by the tensorial product between the angular integral and the coarse level representation of the element stiffness matrices. Thus, the coarsening only needs to be applied directly to the finite element stiffness matrix as follows:

$$\begin{aligned} \left(A^e\right)^C &= P^T A^e P \\ A^C &= \sum_{e=1}^{N} \left(A^e\right)^C \end{aligned} \tag{8}$$

The coarse level spatial stiffness matrices are individually stored and used to create the coarse level matrix ($\boldsymbol{A^C}$) of any moments. This reduces the storage cost since only spatial element stiffness matrices need to be stored at each level. This also allows the efficient matrix vector multiplication in the matrix-free fashion.

The performance of the new preconditioner relative to the MBM and its scalability was studied through the solution of the C5G7MOX benchmark problem [**17**]. Since most of the computational time is spent at the beginning of the computation, only the cpu time for the first power iteration was compared. In order to test the growth rate in the effort, the P_3, P_5, P_7, and P_9

approximations were used with three different spatial resolutions with 29496, 97717 and 174217 nodes respectively. Thus the two higher-resolution problems had increased number of nodes factors of 3.3 and 5.9 node ration relative to the lowest resolution case. Table 1 shows the computational time required for the test cases. The relation between the solution time and the number of nodes for all the test cases are shown in Figure 3.

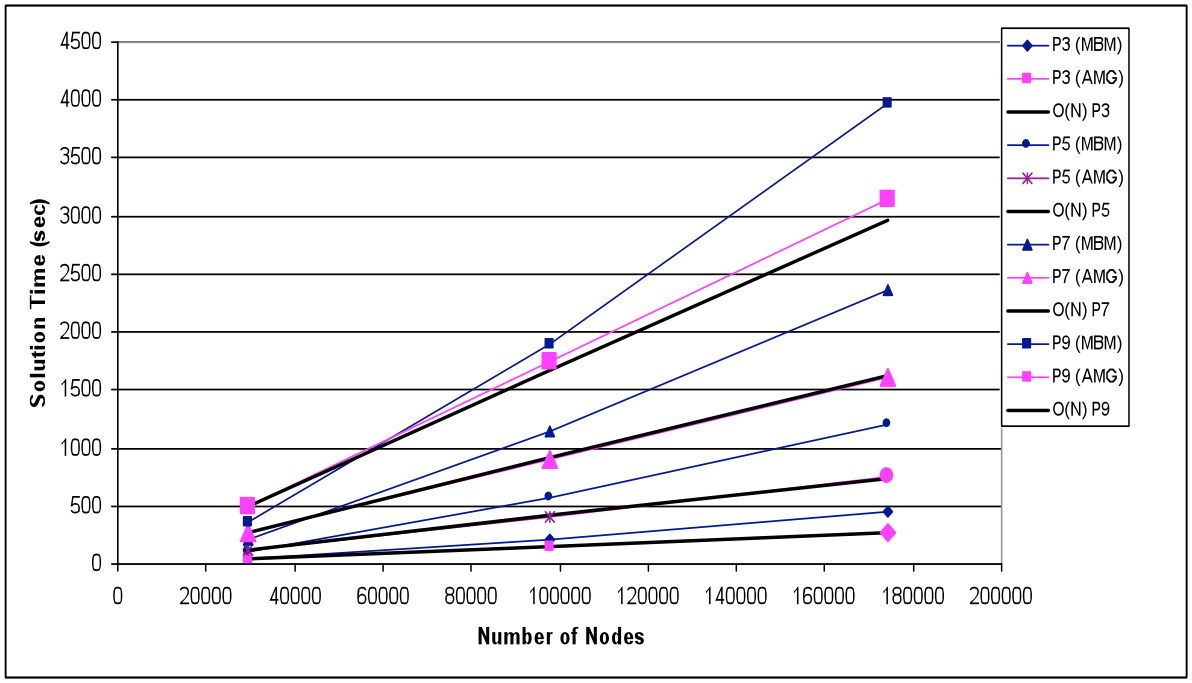

Figure 3. Solution time comparison for C5G7MOX test problem

From Table 2, the scalability of the new AMG preconditioner can be observed for the P_3, P_5, and P_7 cases. The P_9 calculation slightly deviates from the *O(N)* computation time. Even in this case, the solution time grows like $O(N^{1.04})$. On the other hand, the rate of the computational time grows like $O(N^{1.42})$ for the MBM preconditioner. This difference in the growth rate in the solution time indicates the advantage of the AMG preconditioner for the larger system. Table 2 also shows that the MBM preconditioner performs better than the AMG preconditioner for the lowest resolution case. This is due to the size of the diagonal block matrices, which are sufficiently small to be solved very efficiently. However, as the spatial resolution increases, the AMG preconditioner becomes more effective. Figure 3 shows a very encouraging trend since it implies the convergence rate is independent of the mesh size in most of the test cases.

Table 2 Computational time for the test problem with different resolutions

	MBM		*AMG*	
Angular expansion	**Solution time (sec)**	**Relative time increase**	**Solution time (sec)**	**Relative time increase**
29496 nodes				
P_3	44	1.0	47	1.0
P_5	105	1.0	125	1.0
P_7	210	1.0	276	1.0
P_9	360	1.0	503	1.0
97717 nodes				
P_3	213	4.8	149	3.2
P_5	579	5.5	409	3.3
P_7	1137	5.4	906	3.3
P_9	1890	5.3	1747	3.5
174217 nodes				
P_3	457	10.4	274	5.8
P_5	1200	11.4	753	6.0
P_7	2361	11.2	1608	5.8
P_9	3972	11.0	3148	6.3

3.3 Hierarchical Space-Angle Adaptivity

3.3.1 Introduction

Another part of the first year effort was spent to develop an adaptive strategy for the space-angle matrix [**3,4**]. The motivation stems from the fact that spatial heterogeneity in the system produces high anisotropy in the radiation field. This anisotropic radiation flux can be captured only by increasing the order of the angular approximation. On the other hand, the anisotropy in the angular flux is often localized; therefore, in order to minimize the computational effort without sacrificing the accuracy, the adaptive local angular refinements are necessary. This provides a strategy to minimize both computational costs and storage to reach the required accuracy. The refinement strategy developed is based on the hierarchical *p*-adaptivity [**14**] and has been implemented in the code EVENT [**12**].

3.3.2 Numerical Methodology and Results

The finite element-spherical harmonics matrix ***A***, which is based on the second-order, even-parity form of the transport equation, has a shell structure due to the hierarchical nature of the spherical harmonics, and it can be cast in the form:

$$A = \begin{pmatrix} A_{00} & A_{02} & .. & A_{0L} \\ A_{20} & A_{22} & .. & A_{2L} \\ .. & .. & .. & .. \\ A_{L0} & A_{L2} & .. & A_{LL} \end{pmatrix} \tag{9}$$

where $L=N-1$ is the number of spherical harmonics (Legendre) expansion shells for a given P_N approximation. The number of spherical harmonics expansion functions M can be expressed in terms of L by $(L/2+1)^2$, and $(L/2+1)(L+1)$ for two- and three-dimensional geometries, respectively. This hierarchical structure allows addition of shells without changing the existing matrix and this provides the basis for the adaptive angular refinement strategy.

The degree of anisotropy in angular flux varies widely with space and energy groups. A system with heterogeneous regions may produce a highly anisotropic angular flux distribution. This anisotropy can be captured by the numerical solution by increasing the order of the angular approximation. However, often these highly heterogeneous regions do not constitute the whole problem domain, but are largely localized. The angular flux in rest of the domain may be smooth, and thus only require modest number of the angular moments. Uniform refinement of the angular expansion can be, therefore, computationally inefficient, and a local angular refinement strategy is, consequently, more desirable.

The strategy taken here to adapt angular expansion is based on a posteriori error measure for the residual. Given a P_N expansion, the next ℓ-shell in the spherical harmonics expansion is temporarily added to the existing FE-P_N matrix. The residual of the matrix equation is then computed by using the previous solution. The residual is then scaled by the diagonal matrix coefficients in order to obtain an estimate of the solution. This estimate is justified because we assume that the solution of higher spherical harmonics moments is localized in space. The added degrees of freedoms will be kept if the estimates are large enough to affect the scalar flux solution. This leads in effect to a nodal P_N expansion i.e. the angular resolution is different at each node. Interfacing the nodes between the different angular expansion orders is done by simply considering coefficients of the higher moments to be zero.

The accuracy and efficiency of the adaptive angular refinement algorithm was studied by solving the C5G7MOX benchmark problem [**17**]. This is a very challenging problem for fine-mesh transport methods due to the fact that the angular flux changes very rapidly in the fuel-cladding-moderator region. In a previous study very high angular resolution was necessary to achieve the reference eigenvalue result.

The benchmark problem was discretized into 106352 triangular elements with 53585 nodes. The geometry of the problem is shown in Fig. 4(a), and the Fig. 4(b)-(d) shows the contour plots of the moment distributions for the group 1, 4, and 7, respectively. In Fig. 4(b)-(d), the red regions represent the regions where the P_{14} angular expansion was used, and blue regions represent the regions where the angular expansion was truncated at the P_0~P_2 moment. Figure 4(b)-(d) shows that the fuel assembly region requires higher-order angular expansions. The moderator region requires up to a P_3 approximation in group 7. Comparing Figure 4(b) and (d), the higher moment regions covers a much wider area in Figure 4(b). It shows the large neutron leakage around the fuel-moderator boundary.

Figure 5 shows the percentage k-effective errors for the different P_N approximations using both uniform and adaptive angular refinements. Adaptive P_N calculation indicates that the highest order of the spherical harmonics shell (L) required is N-1. Figure 5 clearly shows that same

percent errors in k-effective are achieved with much smaller number of total degrees of freedom in the adaptive angular refinements.

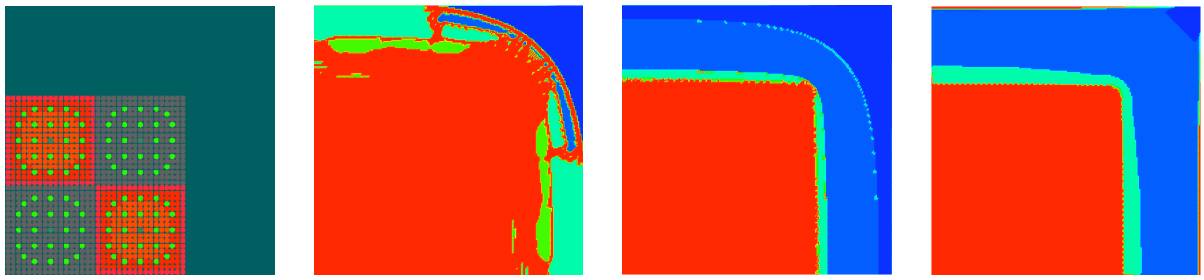

(a) Problem geometry (b) Group 1 (c) Group 4 (d) Group 7

Figure 4. Problem geometry and contour plot of moments

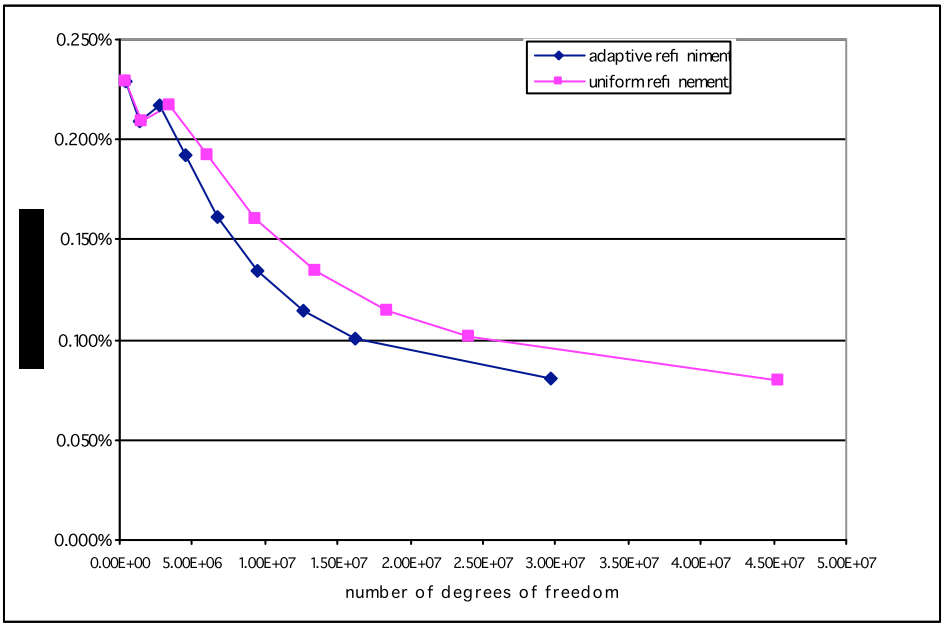

Figure 5. Percent k-effective error vs. number of degrees of freedom.

4. *A Posteriori* Error Analysis for the Second-Order, Even-Parity Transport Equation

4.1. Weak Formulation of the Transport Problem

The one-group, even-parity form of transport equation with an isotropic source is:

$$-\Omega \cdot \nabla G \Omega \cdot \nabla \psi + C\psi = S^{+} \qquad (10)$$

where G and C are the parity collision operators, ψ is the even-parity angular flux and S^+ a prescribed source. Our *a posteriori* error analysis is based on the weak formulation of the problem, which can be represented by the two functionals shown below:

$$F[\phi,\psi] = (\Omega \cdot \nabla\phi, G\Omega \cdot \nabla\psi) + (\phi, C\psi) + \langle \phi,\psi \rangle \tag{11}$$

$$F_s[\phi] = (\phi, S^+) + \langle \phi, T \rangle + (\Omega \bullet \nabla\phi, GS^-) \tag{12}$$

The Finite Element-Spherical Harmonics (FE-P_N) method then seeks the solution $\psi_{h,N} \in V_h x P_N$ such that:

$$F(\phi_{h,N}, \psi_{h,N}) = F_s(\phi_{h,N}) \text{ for all } \phi_{h,N} \in V_h x P_N \tag{13}$$

where, $\psi_{h,N}$ and $\phi_{h,N}$ are the trial and basis functions. V_h and P_N denote the spatial finite element space and the angular expansion spaces, respectively. In order to characterize the discretization error in L_2 norm, we employ the dual problem. The dual problem of Eq. (13) can be expressed as:

$$F^*(z,w) = L(w) \tag{14}$$

where, z and w are the solution and basis functions of the dual problem, respectively. Since Eq. (10) is self-adjoint, $F^*(.\ ,\ .) = F(.\ ,\ .)$. It is a common practice to exploit the adjoint source term to characterize the desired quantity. Suppose we are interested in characterizing the discretization error in the L_2 norm. If we choose an arbitrary adjoint source term $L(w)$ be the even-parity angular flux discretization error in the forward problem $e_{h,N} = \psi - \psi_{h,N}$, then the adjoint source term can be expressed as:

$$L(w) = \int_{4\pi} d\Omega \int_V dV e_{h,N} w \tag{15}$$

The L_2 error norm can then be expressed by substituting discretization error into the adjoint basis function:

$$\left\| \psi - \psi_{h,N} \right\|^2_{L_2(Vx\Omega)} = L(\psi - \psi_{h,N}) \tag{16}$$

Utilizing a standard *a posteriori* error analysis [**9**], one can bound the error as:

$$\left\| \psi - \psi_{h,N} \right\|_{L_2(Ex\Omega)} \le c \sum_E \left(\left\| h_E^2 R(\psi_{h,N}) \right\|_{L_2(Ex\Omega)} + \frac{1}{2} \left\| h_K^{3/2} R_\gamma(\psi_{h,N}) \right\|_{L_2(\partial Ex\Omega)} \right) \tag{17}$$

where $R(\psi)$ represents the finite element (FE) residual of the strong (second-order) form of the problem, h_E is the length of the element E, and c is the constants independent of the

discretization and solution. Thus, we can define the local error indicator (η_E) and global error indicator as follows:

$$\eta_E^2 = h_E^4 \left\| R(\psi_{h,N}) \right\|_{L_2(E x \Omega)} + \frac{h_E^3}{2} \left\| R_\gamma(\psi_{h,N}) \right\|_{L_2(\partial E x \Omega)} \tag{18}$$

$$\eta^2 = \sum_E \eta_E^2 \tag{19}$$

Similar analysis can be applied to obtain the following expression in terms of the energy norm:

$$\eta_E^2 = h_E^2 \left\| R(\psi_{h,N}) \right\|_{L_2(E x \Omega)} + h_E \left\| R_\gamma(\psi_{h,N}) \right\|_{L_2(\partial E x \Omega)} \tag{20}$$

4.2. Extremum Variational Principles and Goal-Oriented Error Bounds

The adaptive strategy together with the global error estimates can optimize the computational effort whilst minimizing the error in the global even-parity flux. On the other hand, it is often the case that the physical parameters of interest in engineering practice are described by local (or global) integral quantities (functional). For example, the power distribution, leakage rate or the effective multiplication constant are often sought for the design of nuclear reactors, while the dose rate to a particular organ may be the most important quantity for the medical physics applications. Therefore, an error indicator with respect to some prescribed engineering or physical output may be more relevant to real-life applications. The aim of this work is to develop error bounds of desired engineering output based on a residual-based *a posteriori* error analysis and the extremum variational principles. The framework is based on the second-order, even-parity form of the transport equation, and uses the extremum variational principle in order to estimate the error in functional outputs. A corresponding extremum (minimum) variational principle of Eq. (10) can be written as [**18**]:

$$\begin{aligned} K^+[\psi] = & \left(\Omega \cdot \nabla \psi, G \Omega \cdot \nabla \psi\right) + \left(\psi, C\psi\right) + \left\langle \psi, \psi \right\rangle \\ & - 2\left(\psi, S^+\right) - 2\left\langle \psi, T \right\rangle - 2\left(\Omega \cdot \nabla \psi, G S^-\right) \end{aligned} \tag{21}$$

where $(.,.) \equiv \int d\Omega \int dV$, $\langle .,. \rangle \equiv \int |\Omega \cdot \hat{n}| d\Omega \int dS$, and T is the surface source. The involutory transformation of the Eq. (21) gives the equivalent extremum variational principles in terms of the odd parity flux:

$$\begin{aligned} K^-[\chi] = & -\left(\Omega \cdot \nabla \chi, C^{-1} \Omega \cdot \nabla \chi\right) - \left(\chi, G^{-1} \chi\right) - \left\langle \chi, \chi \right\rangle \\ & + 2\left(\chi, S^-\right) + 2\left\langle \chi, T \right\rangle + 2\left(\Omega \cdot \nabla \chi, C^{-1} S^+\right) \\ & + (S, GS) + (S, CS) + 2\left\langle T, T \right\rangle \end{aligned} \tag{22}$$

The functionals (21) and (22) are equivalent; therefore, they all have the same extremum value. Due to the self-adjointness of the operators G and C, and the second variation being positive, the extremum value of the functional (21) represents a minimum. On the other hand, the extremum value of the variational principle (22) represents a maximum. Let the extremum value of the functional (21) and (22) be γ. Then, γ is bounded by:

$$K^{-}[\chi] \le \gamma \le K^{+}[\psi] \tag{23}$$

It is, in general, possible to characterize the most of the desired engineering outputs by the product of the forward solution and the adjoint source term. For example, a reaction rate for a particular region can be expressed by setting $S^{+*}=\sigma$, $S^{-*}=0$ and $T^{*}=0$:

$$\begin{aligned} F_s^*[\psi] &= \left(\psi, S^{+*}\right) \\ &= \int_{V_a} dV \int_{4\pi} d\Omega \sigma \psi \end{aligned} \tag{24}$$

The leakage rate through a vacuum surface can be expressed as:

$$\begin{aligned} F_s^*[\psi] &= \left\langle \psi, T^{+*} \right\rangle \\ &= \int_{\Gamma_b} d\Gamma \int_{\Omega \bullet \boldsymbol{n} > 0} d\Omega \left| \Omega \bullet \boldsymbol{n} \right| \psi \\ &= \int_{\Gamma_b} d\Gamma \int_{\Omega \bullet \boldsymbol{n} > 0} d\Omega \left| \Omega \bullet \boldsymbol{n} \right| G \Omega \bullet \nabla \psi \end{aligned} \tag{25}$$

The exact value of the target functional quantity is, then, expressed by the product of the forward and adjoint solutions:

$$F_s^*[\phi^+] = F[\phi^+, \phi^*] \tag{26}$$

Making use of the bilinearity of the functional $F[.,.]$, we can rewrite the RHS of the Eq. (26) as the following linear combination of the quadratic functional:

$$\begin{aligned} F_s^*[\phi^+] &= F[\phi^+, \phi^*] \\ &= \frac{1}{4}\left(F[\phi^+ + \phi^*, \phi^+ + \phi^*] - F[\phi^+ - \phi^*, \phi^+ - \phi^*] \right) \end{aligned} \tag{27}$$

Finally, by utilizing Eq. (27), the target functional value can be bounded by the linear combination of the extremum principles:

$$-K_a^+[\psi + \psi^*] \le F[\phi^+ + \phi^{+*}, \phi^+ + \phi^{+*}] \le -K_a^-[\chi + \chi^*] \tag{28}$$

`

$$-K_b^+[\psi - \psi^*] \le F[\phi^+ - \phi^{+*}, \phi^+ - \phi^{+*}] \le -K_b^-[\chi - \chi^*] \tag{29}$$

$$\frac{1}{4}\left(-K_a^+[\psi+\psi^*]+K_b^-[\chi-\chi^*]\right)\le F_s^*[\phi^+]\le\frac{1}{4}\left(K_b^+[\psi-\psi^*]-K_a^-[\chi+\chi^*]\right) \tag{30}$$

The subscripts *a* and *b* in Eq. (30) indicate the difference from the original variational principles. The source functionals in these variational principles are represented by the linear combination of the forward and adjoint source terms. Note that in order to obtain the bound in Eq. (30), one must solve four problems (forward and adjoint problem of the even- and odd-parity equations).

On the other hand, different *a posteriori* error estimates give the upper and lower bounds of the energy norm. Let us denote the upper and lower bounds of the energy norm be η_{low}^+, η_{up}^+, η_{low}^-, and η_{up}^-, which consist the following bounds:

$$\left(\eta_{low}^+\right)^2\le F\left[se+\frac{\varepsilon}{s},se+\frac{\varepsilon}{s}\right]\le\left(\eta_{up}^+\right)^2 \tag{31}$$

$$\left(\eta_{low}^-\right)^2\le F\left[se-\frac{\varepsilon}{s},se-\frac{\varepsilon}{s}\right]\le\left(\eta_{up}^-\right)^2 \tag{32}$$

By using Eq. (31) and (32), the bound in the error in the target functional can be expressed as:

$$\frac{1}{4}\left(\eta_{low}^+\right)^2-\frac{1}{4}\left(\eta_{up}^-\right)^2\le F_s^*[e]\le\frac{1}{4}\left(\eta_{up}^+\right)^2-\frac{1}{4}\left(\eta_{low}^-\right)^2 \tag{33}$$

Due to the positivity of the quadratic functional, another wider bound can be developed by taking the maximum values of Eq. (31) and (32):

$$-\frac{1}{4}\left(\eta_{up}^-\right)^2\le F_s^*[e]\le\frac{1}{4}\left(\eta_{up}^+\right)^2 \tag{34}$$

In fact the upper bounds η_{up}^+ and η_{up}^- can be estimated by the developed *a posteriori* error estimators, which are the solution of the local residual problem [**19,20**]. The error bound (34) is, therefore, requires only the linear combination of the even-parity forward and adjoint solutions.

By recognizing that the even-parity extremum variational principles provides lower bound and a posteriori error bounds gives upper bounds, the tighter error bounds for the target functional can be obtained as:

$$-\tilde{K}_a^+[\tilde{e}+\tilde{\varepsilon}]\le F[e+\varepsilon,e+\varepsilon]\le\left(\eta_{up}^+\right)^2 \tag{35}$$

$$-\tilde{K}_b^+[\tilde{e}-\tilde{\varepsilon}]\le F[e-\varepsilon,e-\varepsilon]\le\left(\eta_{up}^-\right)^2 \tag{36}$$

$$\frac{1}{4}\left(-\tilde{K}_a^+[\tilde{e}+\tilde{\varepsilon}]-\left(\eta_{up}^-\right)^2\right)\le F_s^*[e]\le\frac{1}{4}\left(\left(\eta_{up}^+\right)^2+\tilde{K}_b^+[\tilde{e}-\tilde{\varepsilon}]\right) \tag{37}$$

4.3. Separation of the Error Components

In the previous two sections, we have derived *a posteriori* error estimators based on the global norms and an arbitrary functional that are dependent on both spatial and angular discretizations. In order to apply *a posteriori* error estimates in the context of adaptivity, the error indicator must distinguish the error components of each independent variable. For instance, we can expand the L_2 error norm in terms of spherical harmonics:

$$\begin{aligned}\left\|\psi-\psi_{h,N}\right\|_{L_2(V\times\Omega)} &= \left\|\sum_{l,m}^{N} Y_{l,m}(\Omega)\left[\psi^{l,m}(\boldsymbol{r})-\psi_{h,N}^{l,m}(\boldsymbol{r})\right]+\sum_{l,m=N+2}^{\infty} Y_{l,m}(\Omega)\psi^{l,m}(\boldsymbol{r})\right\|_{L_2(V\times\Omega)} \\ &= \left\{\int_V dV\sum_{l,m=0}^{N,even}\frac{1}{2}(1+\delta_{m,0})\left[e^{l,m}(\boldsymbol{r})\right]^2+\sum_{l,m=N+2}^{\infty,even}\frac{1}{2}(1+\delta_{m,0})\left(\psi^{l,m}(\boldsymbol{r})\right)^2\right\}^{1/2}\end{aligned} \tag{38}$$

where $e^{lm}(\boldsymbol{r})$ is the error in l-th and m-th spherical harmonic moment at position $\boldsymbol{r}$. The second term represents the angular truncation error. The last line of Eq. (38) is obtained by utilizing the orthogonality relationship of the spherical harmonics. The term $e^{lm}(\boldsymbol{r})$ includes both spatial and angular discretization errors up to P_N; therefore, it does not provide useful information whether the element requires spatial or angular refinement. In order to obtain more useful expression for the adaptivity, we compare the FE-P_N solution with the spatially continuous P_N solution:

$$\begin{aligned}\left\|\psi_N-\psi_{h,N}\right\|_2 &= \left\|\sum_{l,m}^{N} Y_{l,m}(\Omega)\left[\psi^{l,m}(\boldsymbol{r})-\psi_{h,N}^{l,m}(\boldsymbol{r})\right]\right\|_2 \\ &= \left\{\int_V dV\sum_{l,m=0}^{N,even}\frac{1}{2}(1+\delta_{m,0})\left[\tilde{e}^{l,m}(\boldsymbol{r})\right]^2\right\}^{1/2}\end{aligned} \tag{39}$$

where $\tilde{e}^{l,m}(r)$ is the l,m-th spherical harmonics moment spatial discretization error of the P_N approximation. Note that the Eq. (39) contains only the spatial discretization error of FE-P_N approximation. The spatial discretization error in P_N approximation can be approximated by substituting Eq. (39) into the RHS of Eq. (17). In this case, the finite element residual term $R_N(\psi_{h,N})$ is computed by following:

$$R_N(\psi_{h,N}) = \int_{4\pi} d\Omega' \sum_{l=0}^{N,even}\frac{2l+1}{4\pi}P_l(\mu_0)\left(S^+ + \Omega'\bullet\nabla G\Omega'\bullet\nabla\psi_{h,N}^+ - C\psi_{h,N}^+\right) \tag{40}$$

Eq. (40) is substituted to estimate the spatial discretization error of P_N approximation. The angular truncation error of the P_N approximation is then found by projecting the spatially converged solution onto the higher order angular space (i.e. P_{N+2} space). In the next subsection we will discuss the specific strategy to estimate the angular truncation error by an implicit error estimator.

4.3.1. Implicit Error Estimator for the Angular Variables

Once spatial convergence is achieved, the angular truncation error can be estimated using $R_{N+2}(\psi_h)$ as the FE residual term in Eq. (17). Higher-order spherical harmonic moments are then added to the angularly non-converged elements. In theory, this approach gives the strategy to refine the angular variables. There is a difficulty, however, using Eq. (17) as the error indicator for the angular variables. Since the required angular order is dependent solely on the physical problem, not on the spatial discretization, the desirable angular error indicator should be independent of the mesh size. Eq. (17) strongly depends on the mesh size and, therefore, it is not the best error indicator. In this sub-section, we introduce an alternate approach in which the error indicator does not depend on the mesh size. The approach is called an implicit error estimator, as opposed to an explicit estimator derived in the previous section, due to its use of solution of the element-wise matrix equation.

To formulate an efficient implicit error estimator, we make use of the hierarchical property of the spherical harmonics functions. Taking into account the smoothness of the finite element approximation on the element interior, the error in even-parity flux may be written as:

$$-\Omega\cdot\nabla G\Omega\cdot\nabla e_{h,N}+Ce_{h,N}=S^{+}+\Omega\cdot\nabla G\Omega\cdot\nabla\psi_{h,N}-C\psi_{h,N} \tag{41}$$

The corresponding natural boundary condition may be written as:

$$\frac{\partial e_{h,N}}{\partial n}=\frac{\partial\psi}{\partial n}-\frac{\partial\psi_{h,N}}{\partial n} \tag{42}$$

Clearly, imposing an appropriate boundary condition Eq. (42) is not possible due to unknown term ψ. However, it is possible to approximate the gradient term by the finite element approximation:

$$\frac{\partial\psi}{\partial n}\approx\frac{1}{2}\boldsymbol{n}_R\cdot\left(\nabla\psi_{h,N}\big|_R+\nabla\psi_{h,N}\big|_L\right)=\left\langle\frac{\partial\psi}{\partial n}\right\rangle \tag{43}$$

Now the weak formulation of the local element residual problem can be written as the following boundary value problem:

$$\begin{aligned}F(\phi,e_{h,N})&=F(\phi,\psi)-F(\phi,\psi_{h,N})\\&=F_s(\phi)-F(\phi,\psi_{h,N})\\&=\int_{4\pi}d\Omega\int_V dV\phi R(\psi_{h,N})+\int_{4\pi}d\Omega\int_{\partial V}d\Gamma\left(\boldsymbol{n}\bullet\Omega\right)\phi\left\langle G\left(\Omega\bullet\nabla\psi_{h,N}-S^{-}\right)\right\rangle\end{aligned} \tag{44}$$

Eq. (44) is valid for any basis functions ϕ. The error term can be estimated by solving the local finite element matrix with the Neumann boundary condition developed by Bank and Weiser [**11**]. To obtain the angular truncation error of P_N approximation, we simply place the $N+2^{th}$ order spherical harmonics functions as the basis function of Eq. (44) and solve the problem. Notice

that the solution of Eq. (44) is independent of discretization and only depends on the angular expansion orders if the gradient term is well recovered by the averaging Eq. (43).

4.4. Summary: Coupled Space-Angle Adaptive Strategy

The previous sections, we have developed *a posteriori* error bounds based for the global norm and the target functional form. The developed error indicator can be used as guidance for the spatial and angular refinement procedure. The developed coupled space-angle adaptivity algorithm is summarized in Figure 6. The basic strategy is to march through from the lower order angular approximation to the higher order approximations. At each P_N approximation, the spatial convergence is first sought. Then, the spatially converged solution is projected onto the higher order angular spaces to estimate angular truncation errors.

0. Set the angular order to be P_1 (N=1)
1. Calculate the FE-P_N solution ψ_h.
2. Compute the FE residual and estimate the spatial discretization errors (η_E).
3. Refine the spatial element where the error indicator is greater than the specified tolerance, and take care the hanging nodes produced.
4. If all the spatial elements satisfy the convergence criteria, go to Step 5, else go to Step 1.
5. Project the spatially converged P_N solution to the P_{N+2} angular space and solve local residual problem to estimate angular truncation errors.
6. Increase the angular expansion order to N+2 where the angular convergence is not satisfied.
7. If all the elements are angularly converged, or the angular order reaches the specified maximum angular order, stop, else go to Step 1.

Figure 6: A coupled space-angle adaptive strategy

4.4.1. Consideration to the Multigroup Problem

Most of the real-life applications are the multigroup problem. The even-parity transport equation in the multigroup form is not self-adjoint; therefore, *a posteriori* error analysis of this chapter is not exactly valid. However, if we consider the problem as a series of one group problems, then within each group, the problem is self-adjoint. In this case we can perform a similar treatment to the multigroup problem as we treated fission—ignore the discretization error caused by the group-to-group scattering source and estimate the error.

There are two main possible mesh refinement strategies for the multigroup problems. One possible strategy is to apply the adaptive refinement separately on each group. An alternative strategy is to treat a whole group as the one problem and apply adaptive refinement. It seems that the first method is more efficient since the refinement is tuned to a specific group as it is well known that the physics of the fast and thermal groups has different characteristics. The drawbacks of this methodology are the complicated interpolation scheme for the group-to-group scattering and cumbersome data management system. Since a number of groups can easily exceed over a hundred, having the different meshes for each group may not be feasible. Therefore, we choose to use the unified mesh. The errors are computed by the sum of the group-wise errors.

4.5. Numerical Results

4.5.1. Two group eigenvalue problem

We assess the effectiveness of the developed adaptivity framework by a multigroup eigenvalue problem. This is a two-group problem and consists of two homogeneous core regions surrounded by a reflector [**21**]. The geometrical configuration for this problem is shown in Figure 7, and corresponding two group cross sections are listed in the Table 3. The purpose of this problem is to illustrate how the adaptive mesh differs between groups and how it affects overall solution.

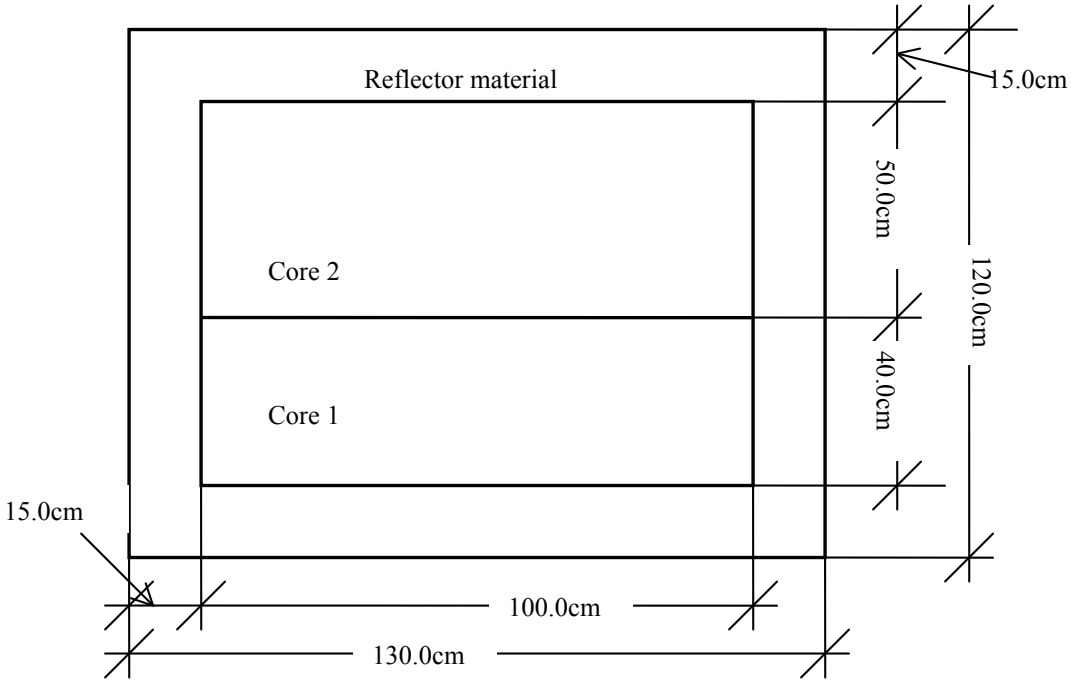

Figure 17: Schematics of the two-group eigenvalue problem

Table 3: Material cross sections of the two group eigenvalue problem (in cm^{-1})

	Core1		Core2		Reflector	
	Group1	Group2	Group1	Group2	Group1	Group2
σ_t	0.2631	0.9416	0.2604	0.8333	0.2950	2.0080
σ_a	0.0121	0.1210	0.0100	0.1000	0.0004	0.0200
$\nu\sigma_f$	0.0085	0.1851	0.0060	0.1500	0.0000	0.0000
χ	1.0000	0.0000	1.0000	0.0000	--	--
σ_s	σ_{s11} 0.2269		σ_{s11} 0.2344		σ_{s11} 0.2453	
	σ_{s12} 0.0241	σ_{s22} 0.8206	σ_{s12} 0.0160	σ_{s22} 0.7333	σ_{s12} 0.0493	σ_{s22} 1.9880

The physics that drives this problem is the fission source in the core regions and the down scatter source in the reflector region. This produces significantly different flux profiles between the two groups. Figures 8 illustrates the flux profile of this problem.

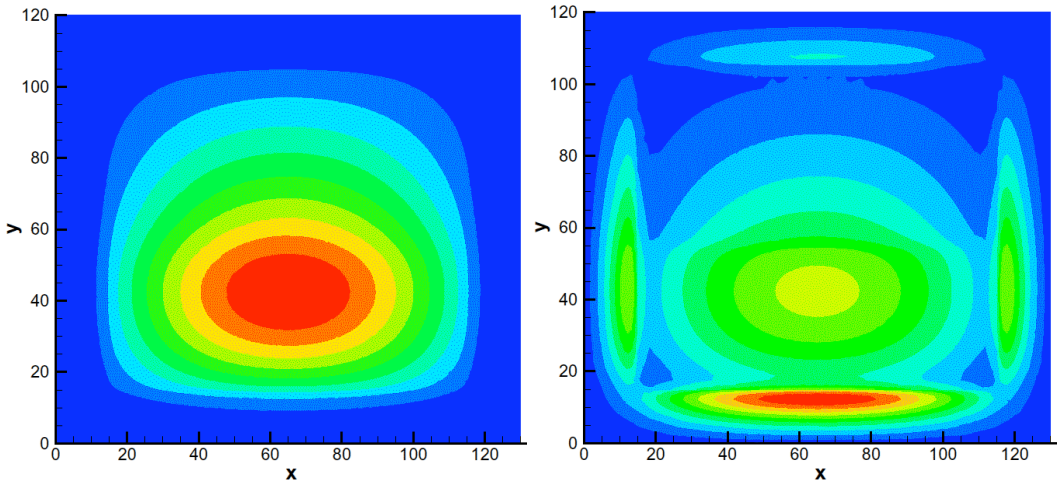

(a) Group 1 (b) Group 2

Figure 8: Flux profile of the two-group eigenvalue problem

Because of the difference in the flux profile, we expect the adaptive mesh refinement to produce the different results in each group. Figures 9(a) and (b) show the initial and final meshes of the diffusion approximation created using different error indicators. The adaptive mesh reflects the difference in physics of the groups. Figure 9(b) shows the adaptive meshes based on the error in the both groups, which somewhat shows the combination of Figures 9(c) and Figures 9(d) as we expected.

In order to see the effect in the solution due to the different adaptive meshes, the number of nodes used for the diffusion approximation solution was compared. The number of the nodes required to converge the effective multiplication constant (k_{eff}) within the 0.01% of converged value (k_{eff} = 1.1422) were 2250, 1778 and 1538 for the error measure based on the first group, second group and both groups, respectively. The differences in the number of nodes are not

significant; a relatively large number of nodes required for the first group originate from the failure of approximating accurate thermal sources around the reflector regions. In order to ensure that all the physics is covered with one error measure, we employ an error measure which is a sum of all groups.

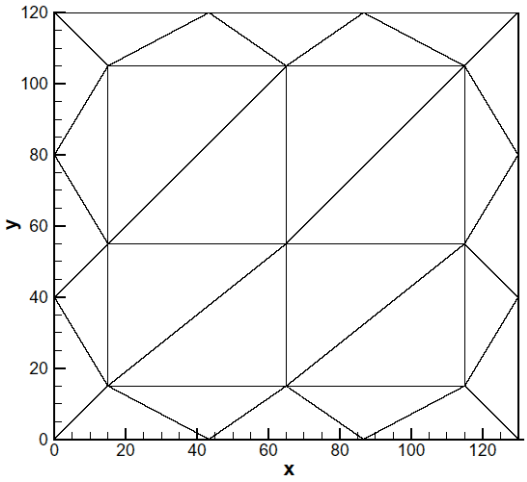

(a) initial mesh

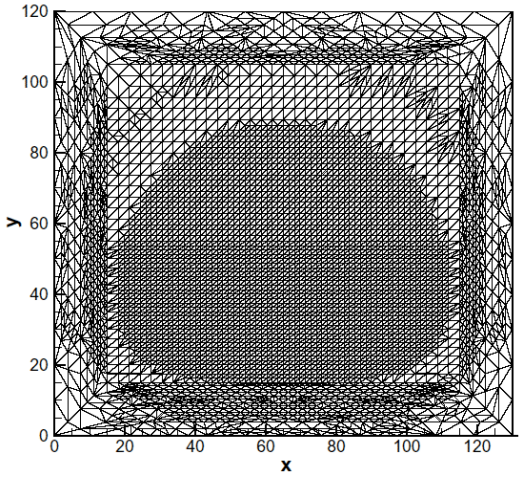

(b) final mesh of adaptivity based on both groups

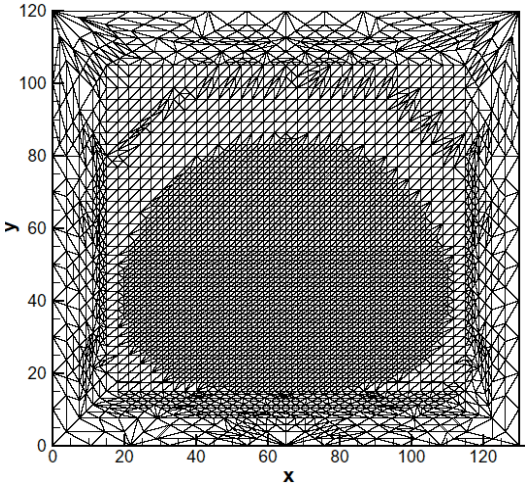

(c) final mesh based on group1 error

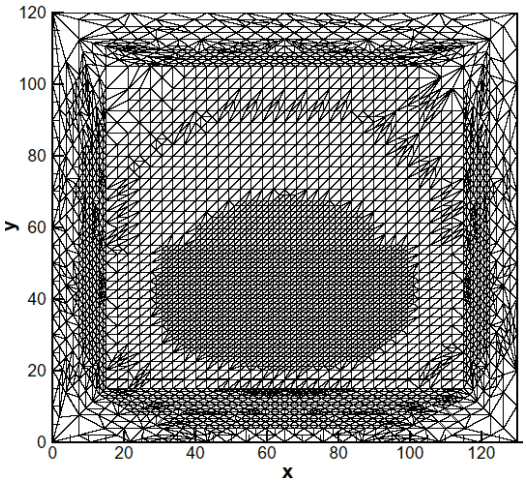

(d) final mesh based on group2 error

Figure 9: Initial and final mesh for the two-group eigenvalue problem

Secondly, we have assessed the convergence behavior of the k_{eff} in terms of number of nodes used in both uniform and adaptive meshes. Figure 10 depicts the percent difference in k_{eff} from the converged values. In order for k_{eff} to converge within 0.01%, the uniform refinement case has required about a factor of 6 more nodes than the adaptive meshes (8717, and 1538 nodes, respectively). This problem is relative large in size, and the important region is somewhat localized; thus, the adaptive strategy shows a greater effect in the mesh refinement.

The difference in the total number of nodes between uniform and adaptive mesh produces a considerable gain in computational time. For example, the k_{eff} converges to the 1.1435 in for a P_9

approximation. To obtain the k_{eff} within 0.01% of this converged value, the adaptive method took 33.5 seconds, while the uniform mesh case took 185.7 seconds. As we see here, the reduction in the number of nodes directly reflects the computational time.

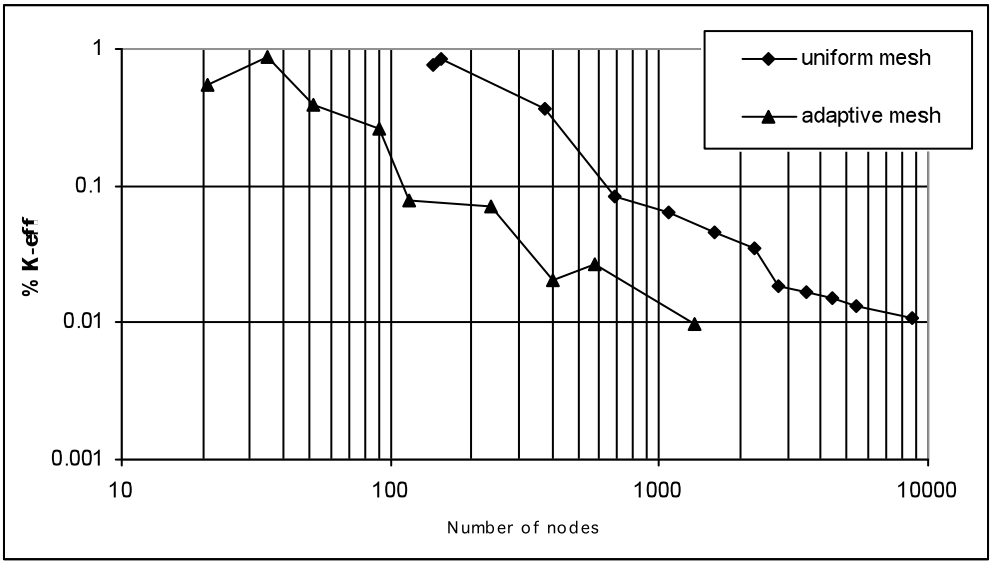

Figure 10: The % k_{eff} difference versus number of nodes

4.5.2. Test Problem for Goal-Oriented Adaptivity

In the previous section, we have tested the adaptivity algorithm and the error measure based on the global L_2 norm. In this subsection, we assess the goal-oriented adaptivity. The problem objective in this case is to estimate the reaction rate of a deep-penetration problem. The problem consists of the 3.0x4.0cm rectangular region with an isotropic beam source shining on the left surface (at x=0.0cm). The region consists of a homogeneous purely absorbing medium with cross section of 1.0cm^{-1}. The quantity of interest is the absorption rate within the region $x \in [0.0,1.0]$, and $y \in [2.0,3.0]$. The problem geometry and cross sections are shown in Figure 11.

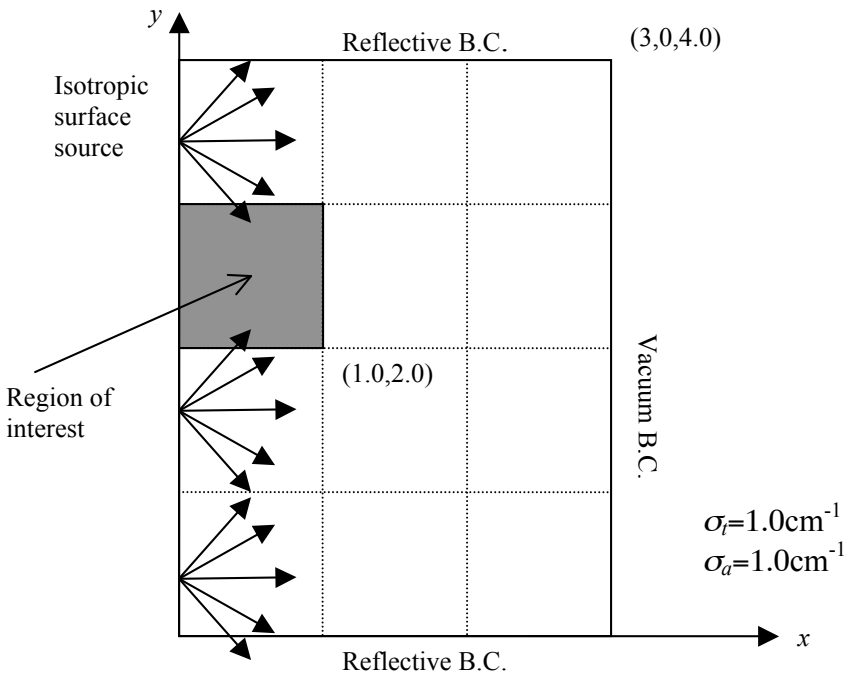

Figure 11: Problem description of deep penetration problem

Due to the reflective boundary condition applied at y=0.0 and 4.0cm, this problem can be considered infinite in the y-direction. Therefore, the problem effectively reduces to the following one-dimensional problem:

$$\begin{aligned} \mu' \frac{\partial \psi}{\partial x} + \sigma\psi &= 0 \\ \psi(0,\mu') &= \frac{1}{2\pi} \quad (\mu' \geq 0) \end{aligned} \tag{1}$$

where, $\mu' = \Omega \bullet \Omega_x$. By solving Eq. (1), the angular flux of the problem is found out to be:

$$\psi(x,\mu') = \begin{cases} \frac{1}{2\pi} e^{-\frac{\sigma x}{\mu'}} & \mu' > 0 \\ 0 & \mu' \leq 0 \end{cases} \tag{2}$$

The reaction rate can be computed by integrating Eq. (2) over the phase space:

$$\begin{aligned} \int_{2.0}^{3.0} dy \int_{0.0}^{1.0} dx \int_{0}^{1} d\mu' \sigma\psi(x,\mu') &= \frac{1}{2} \int_{0.0}^{1.0} dx \int_{0}^{1} d\mu' \, e^{-\frac{\sigma x}{\mu'}} \\ &= E_3(0.0) - E_3(1.0) \end{aligned} \tag{3}$$

The exact reaction rate of the problem is found out to be $\underline{5.5052\text{x}10^{-2}}$. The adjoint problem has the even-parity source of the following form:

$$S^{+*}(x,y) = \begin{cases} \sigma_a & x \in [0.0,1.0] \text{ and } y \in [2.0,3.0] \\ 0 & \text{otherwise} \end{cases} \tag{4}$$

Figures 12(a) and (b) illustrates the forward and adjoint solution of the problem. The location of the adjoint source was chosen so that the adjoint problem would have a dependence on the *y*-direction which reflects on the adaptive mesh generation regardless of the forward problem being effectively one-dimensional. The initial and finial adaptive meshes of the problem are shown in 13.

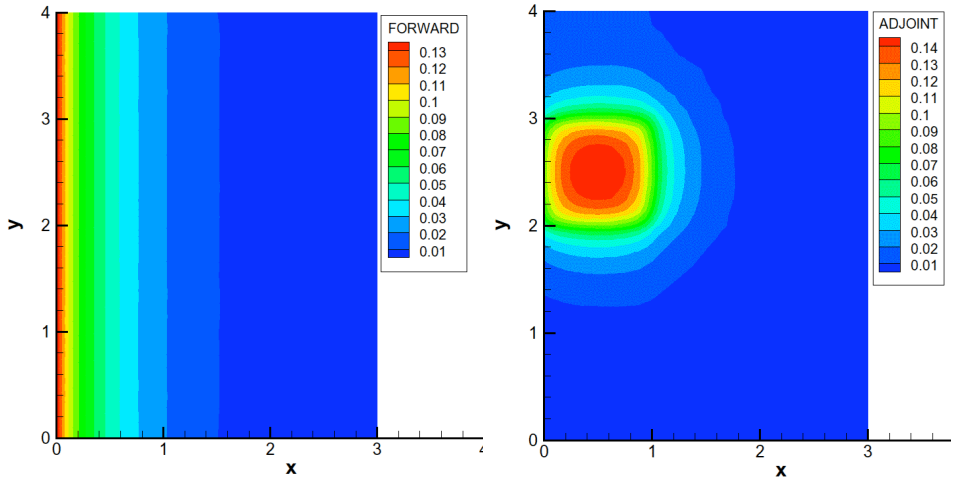

(a) Forward scalar flux (b) Adjoint scalar flux

Figure 12: Forward and adjoint scalar flux for deep penetration problem

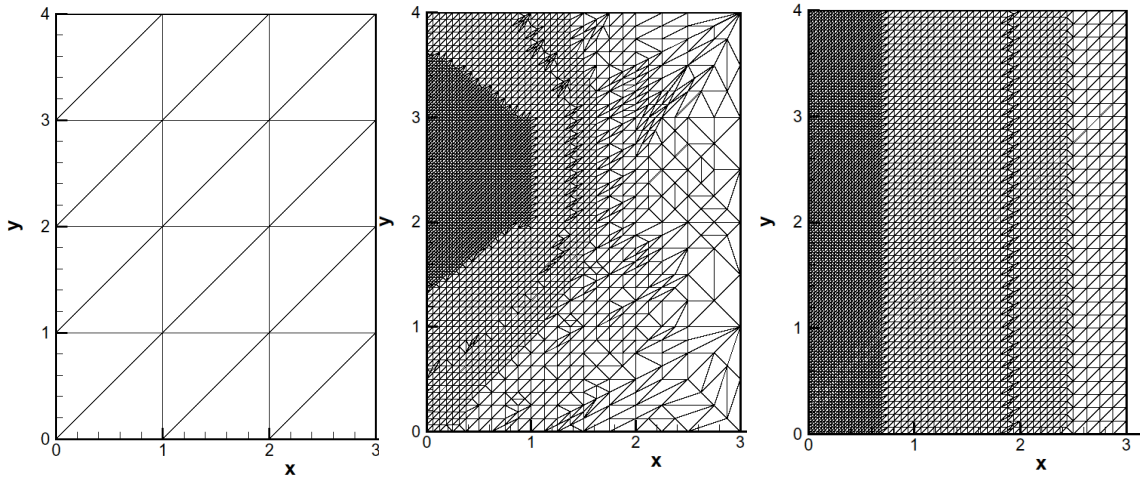

(a) initial mesh

(b) final mesh of the goal-oriented adaptivity (6057 elements)

(c) finial mesh of the global L_2 norm adaptivity (9918 elements)

Figure 13: Initial and finial mesh of deep penetration problem

A clear difference in the final meshes between the goal-oriented and the global L_2 adaptivity can be observed from Figure . As we expected, the adaptivity based on the global L_2 norm has generated the symmetric mesh. On the other hand, it can be clearly seen that the goal-oriented adaptivity is able to identify the region that influences the target functional output. The total number of elements used in the calculations were 6057 and 9918 for the goal-oriented and the global adaptivity, respectively. Both computations were run up to a P_{15} approximation to obtain the error in the reaction rate of $\sim 1.0 \times 10^{-4}$. About 60% less elements were used in the goal-oriented adaptivity. This difference does not appear to be too significant; however, we expect that efficiency of the goal-oriented adaptivity to increase for more complex and larger problems.

An important advantage of the goal-oriented adaptivity is the availability of an error indicator with respect to the target functional. In fact, in order to obtain the reaction rate error of 1.0×10^{-4} by the global L_2 norm adaptivity, a series of calculations with different error indicators were performed. On the other hand, the goal-oriented adaptivity provides the reliable error bounds which can be used as guidance for the termination of the calculation. A summary of the goal-oriented error estimations is listed in Table (without K^+ principle) and Table 3 (with K^+ principle). The last column of Tables 4 and 5 gives the effective indices calculated with respect to the lower bound. In both cases, we observe that the effective indices have become increasingly small.

As we expected, the inclusion of K^+ principle produces sharper bounds. The effective indices computed with K^+ principles are about 20% smaller than that without K^+ principle. For the higher angular orders (i.e. P_{13} and P_{15}), we observe the effective index is fallen below 1.0. This is a consequence of the upper bound of quadratic functionals $F[e+\varepsilon, e+\varepsilon]$, and $F[e-\varepsilon, e-\varepsilon]$ being computed by the restricted angular basis functions, which appear to underestimate the true upper bound for the higher angular order.

Table 4: Error bounds without K^+ principle

Angular Order	Lower Bound	Upper Bound	True Error	Effective Index (w.r.t. lower bound)
P_1	-1.572E-02	1.322E-02	-7.168E-03	2.19
P_3	-2.830E-03	1.914E-03	-1.878E-03	1.50
P_5	-1.061E-03	8.483E-03	-6.899E-04	1.54
P_7	-5.177E-04	4.534E-04	-3.469E-04	1.49
P_9	-2.955E-04	2.702E-04	-2.206E-04	1.33
P_{11}	-1.883E-04	1.755E-04	-1.604E-04	1.17
P_{13}	-1.301E-04	1.224E-04	-1.243E-04	1.05
P_{15}	-9.508E-05	9.000E-05	-1.007E-04	0.94

Table 5: Error bounds for with K^+ principle

Angular Order	Lower Bound	Upper Bound	True Error	Effective Index (w.r.t. lower bound)
P_1	-9.353E-03	6.541E-03	-7.168E-03	1.30
P_3	-2.243E-03	6.061E-04	-1.878E-03	1.19
P_5	-8.609E-04	4.714E-04	-6.899E-04	1.25
P_7	-4.287E-04	3.102E-04	-3.469E-04	1.23
P_9	-2.490E-04	2.020E-04	-2.206E-04	1.13
P_{11}	-1.617E-04	1.376E-04	-1.604E-04	1.01
P_{13}	-1.137E-04	9.902E-05	-1.243E-04	0.91
P_{15}	-8.458E-04	7.463E-05	-1.007E-04	0.84

Tables 6 and 7 show the average error and the difference in the reaction rate between the subsequent angular orders. Comparing Table 6 and Table , although the effective indices are relatively small for all the cases, it can be clearly seen that the average errors computed by the bounds with K^+ principles do indeed represent the difference better. Thus, the inclusion of the K^+ bound does not only sharpen the error bounds, but also shifts the error bounds in the right direction.

Table 6: Average error computed by the bounds without the K^+ principle

P_N	Average Error	P_{N+2}-P_N	Effective Index
1	-1.25E-03	-5.290E-03	0.24
3	-4.58E-04	-1.188E-03	0.39
5	-1.06E-04	-3.430E-04	0.31
7	-3.22E-05	-1.263E-04	0.25
9	-1.27E-05	-6.020E-05	0.21
11	-6.40E-06	-3.610E-05	0.18
13	-3.85E-06	-2.360E-05	0.16
15	-2.54E-06		

Table 7: Average error computed by the bounds with the K^+ principle

P_N	Average Error	P_{N+2}-P_N	Effective Index
1	-1.41E-03	-5.290E-03	0.27
3	-8.18E-04	-1.188E-03	0.69
5	-1.95E-04	-3.430E-04	0.57
7	-5.93E-05	-1.263E-04	0.47
9	-2.35E-05	-6.020E-05	0.39
11	-1.21E-05	-3.610E-05	0.33
13	-7.34E-06	-2.360E-05	0.31
15	-3.86E-04		

5. Summary of Research and Conclusions

5.1. Algebraic Multigrid Method and Nodal-Based Angular Refinement

The initial research focused on two aspects of a general hierarchical adaptive solution strategy, namely, the algebraic multigrid method, and adaptive angular refinement. For the algebraic preconditioner development, we found out that the AMG is effective for the large problems due to its scalability. However, it still needs a user expertise to choose some parameters for the best performance. It was also found out that the AMG is not very effective for small problems because of the large overhead per iterative cycle. More robust, fully-automatic multigrid algorithms would need to be developed. The strategy to choose the most suitable preconditioner for the given problem needs to be further considered.

Research into adaptive angular refinement provided some very promising results. Preliminary results showed that the required angular expansions can be quite different between energy groups. This indicates that the regions of importance are largely energy-dependent. Thus, it may be more effective to perform the adaptive refinements in a group-wise manner by sacrificing the memory usage and cumbersome data management. The angular refinement considered here is based on a nodal-wise refinement approach. A next step would be to develop integrated space-angle refinement method, and an element-wise adaptive approach may be more suitable in this case.

5.2. *A Posteriori* Error Analysis and Coupled Space-Angle Adaptivity

The last body of work focused on the development of a self-adaptive numerical framework based on the residual *a posteriori* error analysis. We have derived the error indicators for both global norm and the arbitrary functional output for the even-parity transport equation. The spatial and angular discretization errors were successfully separated by initially seeking the spatial convergence for a given angular resolution, and subsequently employing a higher-order projection of the spatially converged solution to evaluate the angular truncation error. By utilizing an arbitrary adjoint source, (near) optimal discretization, tuned to minimizing the error in the target engineering output, was accomplished. Numerical results have demonstrated the accuracy and efficiency of the developed adaptive algorithm. The extra computational overhead, which stems from an iterative mesh refinement process, is compensated by the (near) optimum mesh generation.

References

1. Park, Hyong-Kae and de Oliveira, C. R. E., "Algebraic Multigrid Methods for the Solution of the Finite Element-Spherical Harmonics Equations", *Transactions of the ANS*, **91**, (2004), 122-124.
2. Park, Hyong-Kae and de Oliveira, C. R. E., "A Block-diagonal Parallel Preconditioning Strategy for the Finite Element-Spherical Harmonics Method", *Transactions of the ANS*, **92**, (2005), 728-730.

3. Park, Hyong-Kae and de Oliveira, C. R. E., "A Space-Angle Algebraic Multigrid Preconditioner for the Finite Element-Spherical Harmonics Method", (Proceedings of the ANS International Topical Meeting on Mathematics and Computation, M&C 2005, Avignon, France, Sep 12-15, 2005).
4. Park, Hyong-Kae and de Oliveira, C. R. E., "Adaptive Angular Resolution for the Finite Element-Spherical Harmonics Method", *Transactions of the ANS*, **93**, (2005), 517-519.
5. Park, H. and de Oliveira, C. R. E. "Multi-resolution analysis for radiation transport problems" (19th International Conference of Transport Theory, Budapest, Hungary, July 24-30, 2005).
6. Park, Hyong-Kae and de Oliveira, C. R. E., "Coupled Space Angle Adaptivity for Radiation Transport Modeling", *Transactions of the ANS*, **94**, (2006), 514-516.
7. Park, Hyong-Kae and de Oliveira, C. R. E., "Goal-Oriented Error Control for Self-Adaptive Radiation Transport Calculations", *Transactions of the ANS*, **95**, (2006), 588-590.
8. Park, Hyong-Kae and de Oliveira, C. R. E., "Verification of the Coupled Space-Angle Adaptivity Algorithm for the Finite Element-Spherical Harmonics Method via the Method of Manufactured Solutions", (Proceedings of the Joint International Topical Meeting on Mathematics & Computation and Supercomputing in Nuclear Applications, M&C 2007+SNA 2007, Monterey, USA, April 15-19, 2007).
9. Park, Hyong-Kae and de Oliveira, C. R. E., "Coupled Space-Angle Adaptivity for Radiation Transport Calculations", *Nuclear Science and Engineering*, **(**in press**)** (2008).
10. Park, Hyong-Kae and de Oliveira, C. R. E., "Coupled Space-Angle Goal-Oriented Adaptivity for Radiation Transport Calculations using Extremum Variational Principles", (*submitted to Annals of Nuclear Energy*) (2008).
11. Totenberg, U., Oosterlee, C., and Schuller, A., "Multigrid", Academic Press, San Diego, California, (2001).
12. de Oliveira, C. R. E. and Goddard, A. J. H., "EVENT - A Multidimensional Finite Element-Spherical Harmonics Radiation Transport Code", (Proceedings of the OECD International Seminar on 3D Deterministic Radiation Transport Code*s*, Paris, December 01-02, 1996)
13. de Oliveira, C. R. E., "An Arbitrary Geometry Finite Element Method for Multigroup Neutron Transport with Anisotropic Scattering", *Prog. in Nuclear Energy*, **18**, 227 (1986).
14. de Oliveira, C. R. E , Pain, C. C, and Eaton, M., "Hierarchical Angular Preconditioning for the Finite Element-Spherical Harmonics Radiation Transport Method", (Proceedings of PHYSOR 2000 – ANS International Topical Meeting on Advances in Reactor Physics and Mathematics and Computation into the Next Millennium, Pittsburgh, USA, May 7-11, 2000).
15. Diop, C. M., Nimal, J. C., Blum, J. C. and Cagnon, R., "TN12 Shipping Cask Benchmark", NEACRP-A-961 (1989).
16. Füllenbach, and T., Stüben, K., "Algebraic Multigrid for Selected PDE Systems", Elliptic and Parabolic Problems, Rolduc and Gaeta 2001. Proceedings of the 4th European Conference. World Scientific, New Jersey London (2002) 399-410
17. Keller, S. E., and de Oliveira, C. R. E., "Two-Dimensional C5G7 Mox Fuel Assembly Benchmark Calculations Using the FEM-PN Code EVENT", *Prog. In Nuclear Energy*, **45**, (2004) 255
18. Ackroyd, R. T., Finite Element Methods for Particle Transport, John Wiley and Sons, 1997.

19. Prudhomme, S. and Oden, J. T., "On Goal-Oriented Error Estimation for Elliptic Problems: Application to the Control of Pointwise Errors," *Computer Methods in Applied Mechanics and Engineering*, **176** (1999), 313-331.
20. Oden, J. T. and Prudhomme, S., "New Approaches to Error Estimation and Adaptivity for the Stokes and Oseen Equations", *International Journal for Numerical Methods in Fluids*, **190** (1999), 3-15.
21. Stacey, W. Nuclear Reactor Physics, Wiley, New York, 2001.